Possibilities and limitations of the sequential kinematic method for simulating evolutionary plasticity problems

Zhenhao Shi[a,b,*], Maosong Huang[a,b], James P. Hambleton[c]

[a]*Key Laboratory of Geotechnical and Underground Engineering of Ministry of Education, Tongji University, Shanghai 200092, China*
[b]*Department of Geotechnical Engineering, Tongji University, Shanghai 200092, China*
[c]*Department of Civil and Environmental Engineering, Northwestern University, Evanston, United States*

Abstract

Evolutionary plasticity processes, such as ploughing and penetrating, widely exist in many geotechnical engineering applications. The simulation of these processes poses considerable challenges due to the occurrence of large deformations, unsteady nature of the material free surface, and inherent coupling between mechanical response and material geometries. This paper explores the possibility of simulating the first-order response of these processes by using sequential kinematic method (SKM) in combination with simple deformation mechanism. The mechanism consists of rigid elements separated by velocity discontinuities. Computations based on the kinematic approach of limit analysis are sequentially performed to evaluate the most likely deformation mode and update material geometries. An r-adaptive kinematic formulation is used that captures versatile velocity fields by optimizing the geometries of simple kinematic mechanism. The modeling methodology is studied in detail for two typical evolutionary plasticity problems: wedge

[*]Corresponding author. Address: Department of Geotechnical Engineering, Tongji University, 1239 Siping Road, Shanghai 200092, China
Email address: `1018tjzhenhao@tongji.edu.cn` (Zhenhao Shi)

ploughing Tresca material and cylinder penetrating undrained clay. The numerical results obtained by using the SKM are compared against existing analytical and numerical solutions, as well as experimental evidence. The paper demonstrates that evolutionary plasticity problems can be simulated in a conceptually simple way using SKM and highlights the potential pitfalls of this technique.
Keywords: plasticity, large deformation, limit analysis, kinematic method, *r*-adaptivity

1. Introduction

Evolutionary plasticity processes are ubiquitous in geotechnical engineering problems. As an archetypal example, the process of cutting in dry sand emphasizes the essential characteristics of this type of problems (see Fig. 1). They include continuous failure of materials, large deformation, and significant changes in the material free surface. Similar phenomena have been observed from lateral buckling of seabed pipelines (Tian and Cassidy, 2010; White and Dingle, 2011), soil cutting and tillage (McKyes, 1985; Godwin and O'Dogherty, 2007), and locomotion of legged robots and vehicle mobility (Li et al., 2013; Recuero et al., 2017; Agarwal et al., 2019). From a theoretical viewpoint, modeling evolutionary plasticity processes poses considerable challenges due to nonlinearities introduced by large deformations, material plasticity, and contact interactions.

Simple analytical models have been proposed to tackle the problems by considering particular *states* within the entire deformation *processes*, mostly corresponding to the incipient failure and steady states. The first type of these models is developed within the context of tribology as a means to explain the role of asperities in frictional interactions between surfaces undergoing relative motion

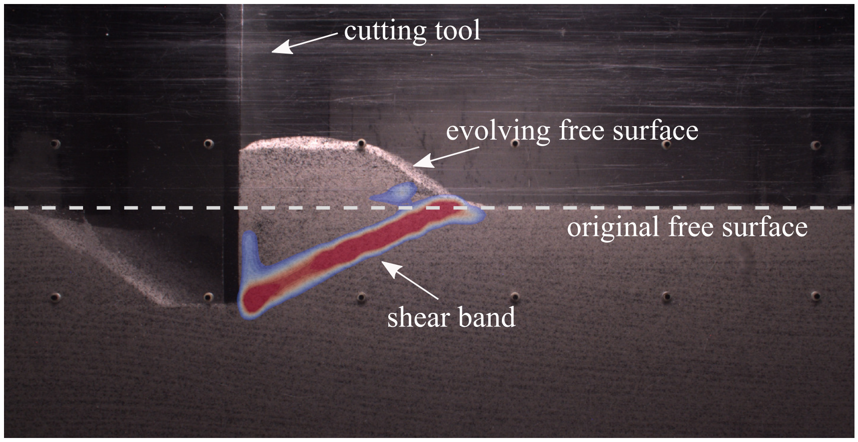

Fig. 1. Deformation pattern and evolution of the material free surface in ploughing a dry sand (Kashizadeh, 2017). Contours shows the intensity of the incremental shear strain interpreted by the PIV analyses (White and Take, 2002; Stanier and White, 2013), with the cooler and warmer colors indicating smaller and larger magnitudes, respectively.

(Collins, 1972; Challen and Oxley, 1979; De Vathaire et al., 1981; Petryk, 1983). These models focus on the steady-state motion characterized by invariant resistance and material surface geometry. The second group of models is developed as tools to predict the loads acting on tillage implements or geotechnical structures (Osman, 1964; Hettiaratchi and Reece, 1974; Perumpral et al., 1983; Godwin and O'Dogherty, 2007). Compared with the former group, these models are mainly interested in the forces required to initiate deformation. When interest is in simulating the complete deformation processes, numerical methods are normally required. For this purpose, various numerical techniques have been used such as large deformation finite element analysis (Bil et al., 2004; Hambleton and Drescher, 2009; Zhang et al., 2015; Ducobu et al., 2016; Zhang et al., 2020; Zhu et al., 2020), discrete element method (Hryciw et al., 1997; Tsuji et al., 2012), and meshfree methods (Leon Bal et al., 2018; Agarwal et al., 2019; Afrasiabi et al., 2019). These approaches achieve considerable success in handling large deformation and the evolving material free surface but tend to be computationally onerous and overly demanding for routine engineering practice.

The sequential kinematic method (SKM) represents a compelling alternative strategy for modeling evolutionary plasticity processes due to its computational efficiency and stability. The technique regards a deformation process as a sequence of failure states, and in each state, the kinematic theorem of limit analysis (Drucker et al., 1952) is applied to compute an optimal velocity field that is subsequently used to update the material geometries. The computational efficiency and stability of SKM has been illustrated in different engineering problems such as structural collapse (Yang, 1993; Corradi and Panzeri, 2004), metal forming (Hwan, 1997; Raithatha and Duncan, 2009), structural geology (Cubas et al., 2008; Mary et al., 2013), and the simulation of penetration, ploughing, and cutting processes in soils (Hambleton, 2010; Hambleton and Drescher, 2012; Hambleton et al., 2014; Kashizadeh et al., 2015; Kong, 2015; Kong et al., 2018; Zhu et al., 2020). Existing SKM formulations evaluate deformations of the entire computational domain. However, in many problems with engineering relevance, the induced deformation tends to be confined to local regions adjacent to the moving object. In the example depicted in Fig. 1, strains are locally concentrated into a single shear band, and the majority of the bulk materials mainly remains stationary or undergoes rigid body motion. Therefore, the SKM formulation that accounts for the deformation within the entire material domain can be unnecessarily complex and computationally inefficient, especially when the primary interest is a quick prediction of the first-order response such as the forces and motion of the moving object.

This paper explores the possibilities of performing a first-order analysis for evolutionary plasticity problems by utilizing SKM in combination with simple kinematic mechanism. In the proposed approach, only deformation adjacent to the moving object is considered and represented by mechanism consisting of sliding rigid elements separated by velocity discontinuities. To allow for versatile velocity fields, the model incorporates an r-adaptive kinematic method operating on the simple mechanism (Shi and Hambleton, 2020). Rather than discretizing the entire domain, the model relies on discretizing solely the material free surface. The modeling methodology is examined for two evolutionary plasticity problems: wedge ploughing Tresca material and cylinder penetrating undrained clay. The simplicity of these problems is appealing from fundamental perspective, and well-documented experimental observations as well as analytical and numerical solutions enable a detailed assessment of the strength and weakness of the proposed technique.

2. General modeling strategy

We employ the problem of wedge ploughing as an archetypal example for conveying the bases of the proposed SKM technique. An object (here a rigid wedge) is pushed into a Tresca solid (Fig. 2(a)), followed by a lateral movement that continuously deforms the cohesive material (Fig. 2(b)). We generally are interested in the forces acting on the moving object (i.e., N and T in Fig. 2) and/or its trajectory. This benchmark problem contains mechanical features that are common to other evolutionary plasticity processes (e.g., see Fig. 2(c) and (d)). First, the material deformed and displaced by the wedge accumulate along the front flank that leads to changes in the free surface (see Fig. 2(b)), alters the deformation patterns of the plastic solid and eventually the resulting forces on the

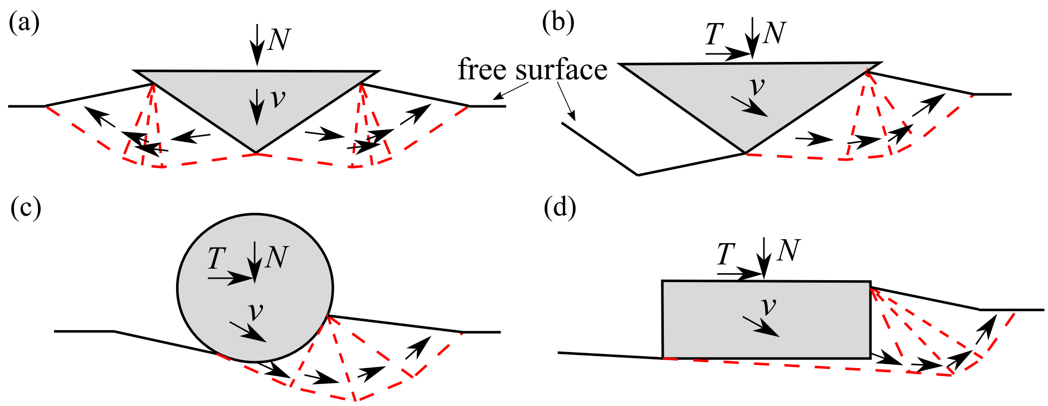

Fig. 2. Schematic illustrating (a) penetrating a plastic solid by a rigid wedge and (b) subsequent ploughing process; (c) ploughing process with circular and (d) rectangular tools.

wedge. Second, the contact conditions between the wedge and its surrounding material evolve as the ploughing proceeds. The full attachment along both flanks during the initial indentation changes to a separation at the rear flank (see Fig. 2(b)). Our general strategies to tackle these challenges by utilizing SKM are summarized in the following. These general modeling strategies can be extended to other problems, as illustrated by the later example of cylinder penetration in undrained clay.

As shown in Fig. 3, we describe the velocity fields of the materials surrounding the wedge by an assembly of rigid elements that only translate in space. The edges of these elements represent velocity discontinuities. In general, the mechanisms could be more complex (e.g., including deformable elements and discretizing entire material domain, see Kong et al. (2018); Zhu et al. (2020)). Nevertheless, the aforementioned deformation pattern reduces the number of unknowns required to constrain kinematic mechanism. It is also consistent with the patterns of concentrated deformation revealed in many evolutionary plasticity processes (e.g.,

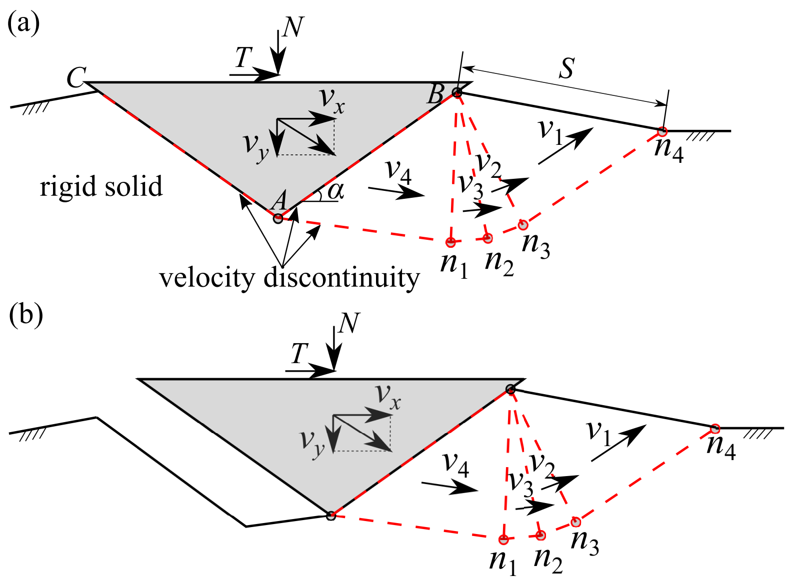

Fig. 3. Schematic illustrating deformation mechanism: (a) at the initiation of wedge ploughing, there are solid-tool interfaces at both front and rear flanks of the wedge; (b) after detaching from solid, there is no interface at the rear flank.

see Fig. 1 or those shown by White and Dingle (2011), Xu and Zhang (2019)). Two types of control can be included in the SKM: prescribing wedge velocity and applying force. Under velocity control (also the common mode of running the SKM), the forces acting on the wedge are evaluated by applying the kinematic theorem of limit analysis. The corresponding material velocity fields are employed to update the material free surface. Under force control, the aforementioned running mode can be iteratively executed for different trial displacements until the targeted force application is reached. It is also possible to jointly control force and velocity for different degrees of freedom of the object (i.e., mixed control). Taking wedge ploughing as an example, the vertical force acting on the tool (i.e., N in Fig. 3) and its horizontal velocity (i.e., v_x in Fig. 3) can be prescribed, while the vertical velocity (i.e., v_y in Fig. 3) and horizontal force (i.e., T in Fig. 3) are recovered as part of the solution.

To actually solve the problem, we have made the following specific assumptions. The plastic solid is assumed to be weightless, rigid-perfectly-plastic, and obeys the Tresca yield criterion and an associative flow rule. Although this constitutive relation is originally proposed for metals, it has been shown to also reasonably approximate the mechanical behavior of cohesive soils (e.g. undrained clay) (Randolph and Houlsby, 1984; Einav and Randolph, 2005; Kong et al., 2018; Zhu et al., 2020). Deformation is considered to be under plane strain conditions. Regarding the wedge ploughing example, this assumption applies to the cases where the out-of-plane dimension of the wedge is much larger than the penetration depth. On the other hand, plain-strain cylinder penetrating can be a reasonable representation of the T-bar penetrometer test used in geotechnical site exploration, where the longitudinal dimension of the penetrometer is often much greater than its in-plane ones.

Detailed descriptions of the kinematic mechanisms utilized for the wedge ploughing problem are given in Fig. 3. In particular, Fig. 3(a) and (b) depict the mechanisms applying to the cases where the rear flank of the wedge (i.e., AC in Fig. 3) is in contact with the Tresca solid and the flank has been detached from its neighboring material, respectively. In light of experimental observation (e.g., Challen et al. (1984)), this work postulates that the material adjacent to the rear flank of the wedge is rigid during ploughing (i.e., only material deformation at the front flank is described by the rigid block mechanism). Accordingly, the only difference between the kinematic mechanisms in Fig. 3(a) and (b) is that the edge AC is treated as a velocity discontinuity in the former case. It should be noted that the aforementioned simplification is made to retain the simplest form of the solution (e.g., less blocks in the mechanism) such that the most clarity on the possibilities and limitations of SKM can be obtained. Indeed, there is no difficulty in adopting a more complex mechanism that would allow for deformation within the material at both sides of the tool. In fact, our preliminary studies show that both simplified and complex mechanisms yield the same results and in the latter case practically zero-valued velocities are computed for the material adjacent to the rear flank of the wedge.

In the following sections, detailed formulation of the SKM will be presented. Specifically, Section 3 discusses the *r*-adaptive kinematic method that is used to construct optimal velocity fields in combination with rigid block mechanism. The approach to update the material geometries based on computed velocity fields will be presented in Section 4.

3. Formulation of *r*-adaptive kinematic method

In this section, we will discuss, for the kinematic mechanism depicted in Figure 3, how an optimal velocity field and the corresponding forces acting on the wedge can be obtained by utilizing the *r*-adaptive kinematic method. The velocity field of Fig. 3 is constrained by two types of information: the geometries of the rigid elements and their velocities. In *r*-adaptive kinematic methods, both block velocities and their nodal positions are treated as variables subjected to optimization (Johnson, 1995; Milani and Lourenço, 2009; Hambleton and Sloan, 2013). For this purpose, the proposed model constructs a nested optimization procedure that in the inner level determines the optimal velocities for a *fixed* mesh by second-order cone programming (SOCP), and at its outer level computes an optimal set among *variable* nodal positions using non-linear optimization. Respectively, these two optimization layers are detailed in sections 3.1 and 3.2. This r-adaptive kinematic formulation closely resembles that described by Shi and Hambleton (2020) for computing limit states of three-dimensional plasticity problems with fixed material geometries.

3.1. Optimization of velocity field for fixed mesh

For a velocity field characterized by rigid elements, the total energy dissipation rate equals to the sum of those occurring at element edges (i.e., the velocity discontinuities). The latter, for a perfectly plastic material that obeys the Tresca yield criterion, can be expressed as (cf. Chen (1975)):

$$\dot{d} = cl|\Delta v_t| \tag{1}$$

The variable l denotes the length of discontinuity, c is the material cohesion, and Δv_t is the tangential velocity jump along element edge. The absolute value is prescribed so that the dissipated power is always positive, regardless of the shearing direction. In a plasticity system as considered by the current SKM formulation, plastic deformation all takes place in velocity discontinuities where strain rates are infinite (Chen, 1975). To account for strain rate effects, the present formulation might be extended by following the approach proposed by Randolph (2004) and Einav and Randolph (2005). The general idea is to introduce a thickness for velocity discontinuities such that finite strain rates can be defined. Then, a relationship between material cohesion (i.e., c in Eq. (1)) and strain rate (e.g., see Dayal and Allen (1975), Ladd and Foott (1974), and Einav and Randolph (2005)) can be included. After including these additional relationships, the energy dissipation rate of Eq. (1) is a function of both the magnitude of velocity jump and the aforementioned thickness. This latter geometry might be determined by seeking a minimization of the energy dissipation rate (i.e., following the principal of minimum work for this term in isolation) (see Randolph (2004) and Einav and Randolph (2005) for detailed discussions on this aspect).

To preserve a linear objective function in the SOCP, $|\Delta v_t|$ in Eq. (1) is replaced by a dummy variable μ:

$$\begin{aligned} \dot{d} &= cl\mu \\ \mu &\geq \sqrt{(\Delta v_t)^2} \end{aligned} \tag{2}$$

The constraint specified in Eq. (2) is in the form of second-order cone (SOC) constraint, one of the types permitted in SOCP in addition to linear equality and inequality constraints (cf. Sturm (2002)). Eq. (2) recovers the exact energy dissipation relation when equality is achieved. For the problems presented in this paper, this condition is always satisfied. This, as will become readily apparent, is because that the SOCP is formed such that the dummy variable μ is minimized. For materials that obey the Tresca yielding criterion and associative flow rule, a kinematically admissible mechanism does not permit velocity jumps that are normal to element edges (Chen, 1975):

$$\Delta v_n = 0 \tag{3}$$

In accordance with the kinematic theorem of plasticity (Drucker et al., 1952), a bound on limit load can be obtained by equating the rate of energy dissipation $\dot{D}$ computed from a kinematically admissible velocity field to the rate of work due to external forces $\dot{W}$ constructed based on the same field. Such energy balance, for the system defined in Fig. 3, can be specified as

$$\dot{W} = Tv_x + Nv_y = \dot{D} = \sum_{i=1}^{N_E} cl_i\mu_i + \sum_{j=1}^{N_I} c_a l_j \mu_j \tag{4}$$

where v_x and v_y denote the velocity of the wedge along x-axis and y-axis, respectively, N_E is the number of velocity discontinuities within plastic materials, and the subscript i is used to indicate quantities corresponding to the i^{th} discontinuity edge. The second energy dissipation term in Eq. (4) accounts for those occurring at the interfaces between the wedge and the plastic solid and thus implying that the wedge and the cohesive mass are treated as a composite dissipative mechanical system. The variable N_I is the number of the interface segments. The dissipation at these interface segments is computed by replacing the cohesion c in Eq. (2) with the interface strength c_a. Perfectly smooth and rough interfaces are characterized by $c_a = 0$ and $c_a = c$, respectively. A simple contact search algorithm is used to determine the range of the interface, where the distance from nodes on the free surface to the wedge flanks is computed and those with a distance less than a tolerance (1.5×10^{-2} is employed for all simulations in this paper) are considered to be in contact with the wedge. Conversely, the separation of the wedge from neighboring plastic solid is naturally considered once the distance exceeds the tolerance mentioned above. To enable such no-tension interface, a jump condition that is slightly different than the one given in Eq. (3) is assigned to the interface segments:

$$\Delta v_n \geq 0 \tag{5}$$

As depicted in Fig. 4(a), the velocity jump at the interface is measured from the wedge to the neighboring plastic material such that a positive value of Δv_n indicates the separation. The interface behavior described by using Eqs. (1) and (5) (see Fig. 4(b)) is similar to that obtained by imposing no-tension conditions with respect to the tractions along the surface of a Tresca solid (e.g., the Type A interface defined by Herfelt et al. (2021)). This approach is not perfect in

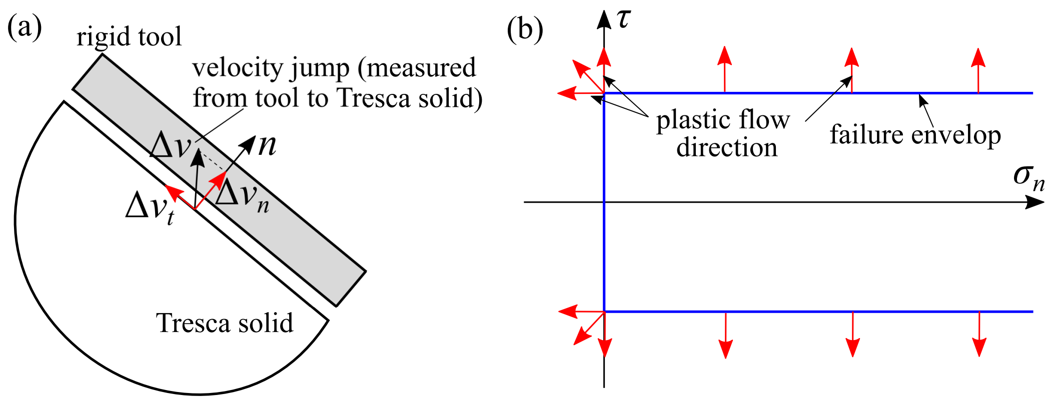

Fig. 4. Schematic illustrating the modeling of non-tension interface between rigid tool and Tresca solid in SKM: (a) interface is treated as velocity jump (measured from tool to Tresca solid); (b) plastic flow directions and failure envelop at the interface.

that it can imply tensile stress states within plastic solid and that shear stress is sustained (i.e., energy dissipation is non-zero) immediately after separation (i.e., at the instance when Δv_n turns positive) (Herfelt et al., 2021; Houlsby and Puzrin, 1999). Nevertheless, it provides a practical means to account for the no-tension interface via the types of constrains permitted by the SOCP. Lastly, it should be noted that the aforementioned limitations mainly influence the instance of separation, after which the interface does not exist any more and consequently is not included in the computation.

By manipulating Eq. (4), we obtain the following optimization problem with respect to the velocities of the rigid elements:

$$
\begin{aligned}
min \quad & T = \frac{1}{v_x}(\sum_{i=1}^{N_E} cl_i\mu_i + \sum_{j=1}^{N_I} c_a l_j \mu_j - N v_y) \\
& or \\
& N = \frac{1}{v_y}(\sum_{i=1}^{N_E} cl_i\mu_i + \sum_{j=1}^{N_I} c_a l_j \mu_j - T v_x) \\
s.t. \quad & \Delta v_{ni} = 0 \\
& \mu_i \geq \sqrt{(\Delta v_{ti})^2} \quad i = 1, ..., N_E \\
& \Delta v_{nj} \geq 0 \\
& \mu_j \geq \sqrt{(\Delta v_{tj})^2} \quad j = 1, ..., N_I
\end{aligned}
\tag{6}
$$

Equation (6) represents a standard form of SOCP problems and depending on whether the ploughing or the indentation process is modeled, the first or the second objective function is employed. The SOCP is solved by the Mosek toolbox integrated with the MATLAB (Mosek, 2015). N and v_y, T and v_x represent two work-conjugate pairs. In order to obtain feasible and bounded solutions from the SOCP, at least one variable in each pair should be specified (e.g., the normal force N and the horizontal velocity v_x are usually the boundary conditions in modeling the ploughing). As only rate-insensitive materials are considered in this work, when setting boundary conditions by prescribing v_x or v_y, a velocity of unity is assigned for convenience.

Equation (6) represents the inner layer of the nested optimization and the computed limit loads correspond to the rigid block mechanism with fixed geometries. The outer layer of the nested optimization, as detailed in the next section, seeks optimal nodal positions of the elements (i.e., nodes n_1 to n_4 in Fig. 3(a)) that minimize the limit loads.

3.2. Optimization of nodal positions of rigid elements (r adaptivity)

To obtain a critical layout of the velocity discontinuities, we construct the following non-linear optimization problem:

$$\begin{aligned} min \quad & F(x_{ij}, S) \quad i = 1,2 \quad \text{and} \quad j = 1,2,3 \\ s.t. \quad & A_k(x_{ij}, S) \geq 0 \quad k = 1,...,4 \\ & x_{ij}^l \leq x_{ij} \leq x_{ij}^u \\ & S > 0 \end{aligned} \tag{7}$$

The objective function in Eq. (7) is the limit tangential or normal force computed for a given set of nodal positions x_{ij} (the first subscript denotes the i^{th} component of the position vector, while the second subscript indicates the j^{th} node), evaluated in precisely the same way as in the previous section. The coordinates of the nodes n_4 in Fig. 3 cannot be regarded as independent unknowns in the optimization since this node has to lie on the material free surface. We implicitly define the location of this node by an auxiliary variable S that measures the distance between the node n_4 and the intersection point of the wedge and the free surface (i.e., the point B in Fig. 3). To prevent the inter-penetration of rigid elements and consequently ensure computational stability, the first set of constraints in Eq. (7) requires that element areas A_k are always positive. The variables x_{ij}^l and x_{ij}^u appearing in the second set of inequality constraints define allowable limits for certain nodal position components. These constraints are set to ensure that the adjusted nodes do not go beyond the material free surface.

As the objective function and constraints of Eq. (7) are both non-linear functions of the unknown variables, such problem falls within the general domain of non-linear constrained optimization. In preliminary studies, two of the most widely employed algorithms, interior point method and sequential quadratic programming, are used to solve this optimization through the FMINCON solver of MATLAB. These initial investigations show that the interior point method can find a solution with fewer iterations and thus are selected for all computations presented in this paper. Three key parameters that can affect the performance of the interior point method are (1) step size factor Δs in finite difference method that determines the perturbation amount of unknown variables for numerically computing the gradient of the objective function; (2) step tolerance T_s that specifies the lower bound on the change of the norm of the vector containing all unknown variables; (3) the tolerance for the optimality T_o that measures the proximity of the current solution to an optimal one. The first parameter affects the accuracy of the calculated gradient of the objective function, while the latter two mainly influence the accuracy of the solution as the optimization process will be terminated once either tolerance is triggered. For simulations performed in this work, we observe that the solutions are not particularly sensitive to the values of Δs and T_o, and their default values (i.e., $\Delta s = 1 \times 10^{-6}$ and $T_o = 1 \times 10^{-6}$) are adopted. The parameter T_s, on the other hand, can noticeably influence the computed response, as it will be discussed more deeply in the following. For all examples considered in this work, $T_s = 1 \times 10^{-4}$ to 1×10^{-5} are sufficient. Lastly, it should be noted that the algorithm used to solve the non-linear optimization is deemed as a local optimizer and therefore behave most effectively when the initial nodal positions of the rigid elements (e.g., Fig. 5(a)) are relatively close to optimal ones (e.g., Fig. 5(b)) or the objective function is convex.

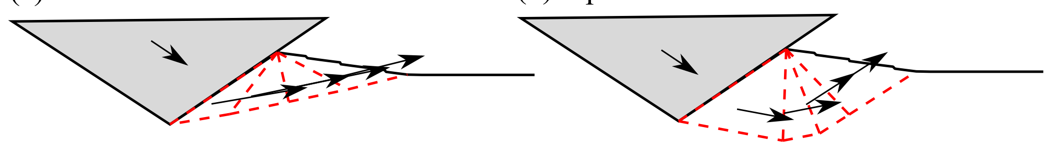

Fig. 5. Typical evolution of kinematic mechanism during r-adaptive kinematic method.

4. Update of material free surface

As shown in Fig. 6(a), deformation of the entire bulk material is tracked through a discretized free surface. By doing so, the need to repeatedly remesh the computational domain, as a means to handle severely distorted mesh, can be avoided. The surface initially has uniform nodal spacing denoted by Δx. The optimal velocity fields obtained in accordance with the technique discussed in the previous section are used to update the displacements of the nodes along the free surface by explicit time integration. Consider a pseudo time increment ΔT_n and let the superscripts $n-1$ and n denote quantities at the pseudo time T_{n-1} and T_n ($T_n = T_{n-1} + \Delta T_n$), respectively. With one-step time-marching scheme, nodal displacements at the end of the increment ΔT_n is found to be:

$$d_{ij}^{n} = d_{ij}^{n-1} + v_{ij}^{n-1}\Delta T_n \quad i = 1,2 \quad \text{and} \quad j = 1,2,\ldots \tag{8}$$

where d_{ij} and v_{ij} denote the i^{th} component of the displacement and velocity vectors at the j^{th} node. For nodes belonging to multiple blocks (e.g., the point B in Fig. 6), an averaged velocities of those blocks are assumed to be nodal velocity (see Fig. 6(b)). Similarly, the position of the rigid wedge is updated according to

$$d_{iw}^{n} = d_{iw}^{n-1} + v_{iw}^{n-1}\Delta T_n \quad i = 1,2 \tag{9}$$

where d_{iw} and v_{iw} represent the displacement and velocity vectors of the rigid wedge. Once the geometry of the free surface and the position of the wedge have been updated, the contact between the wedge and its neighboring materials is checked based on the searching algorithm discussed in Section 3 and the portions of the material free surface that are in contact with the wedge are treated as velocity discontinuities within the kinematic mechanism.

As the size of the time increment is finite, some nodes on the free surface may penetrate the object after the update described above, thus requiring correcting the free surface. Following Kong (2015), those nodes that invade into the interior of the object are mapped back to the boundary of the object along a direction normal to the boundary, as illustrated in Fig. 7(a). Another type of free surface that requires appropriate correction is the sharp inverse corner depicted in Fig. 7(b). Without treatment, the computed boundary between the deforming and stationary materials can be forced to pass the tip of the corner, which represents a local minimum for the objective function (recall that the nature of the selected algorithm is a local

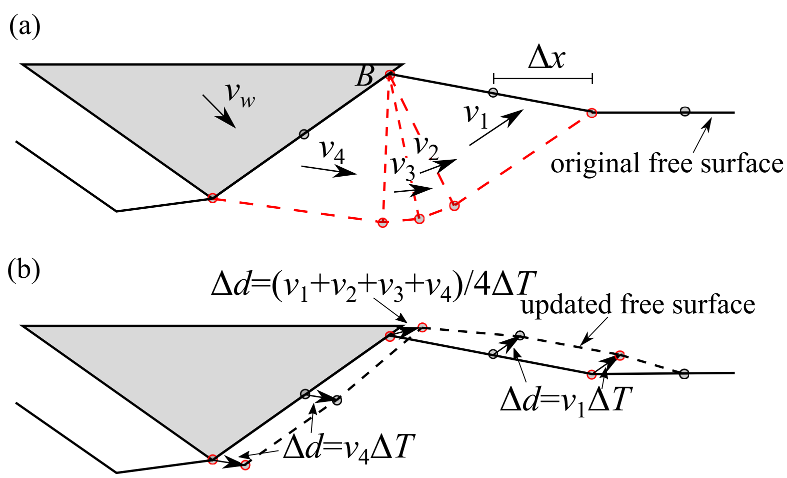

Fig. 6. Schematic illustrating the update of the material free surface according to the computed velocity field: (a) velocity field obtained for geometry configuration at step n; (b) updated free surface and geometry configuration at step $n + 1$.

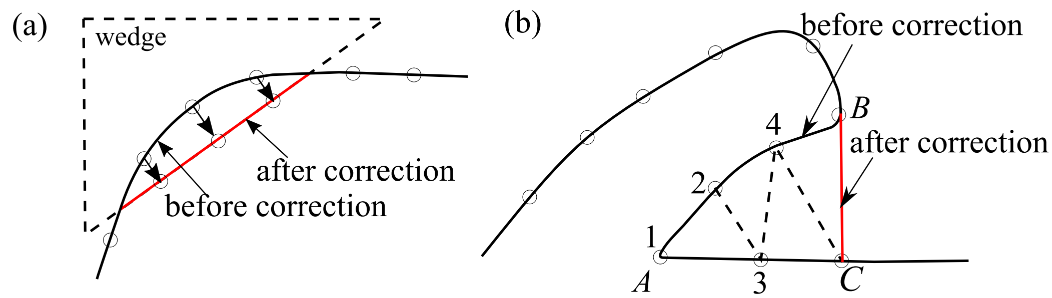

Fig. 7. Schematic illustrating the correction of the material free surface for: (a) penetration into the tool; (b) sharp inverse corner.

optimizer). This behavior prevents searching for better deformation mechanisms, and consequently lead to peculiar jumps on the ploughing resistance and unrealistic deformation patterns, as will be discussed in the following. To resolve this issue, we loop over all surface nodes and delete those whose x coordinate is less than that of its two neighboring nodes, as suggested by Kong (2015). Figure 7(b), in which the number adjacent to nodes indicate the order of being deleted, shows that by repeatedly checking surface nodes and applying the rule described above, the shape corner can be eliminated. Lastly, it should be noted that the need to correct the surface profile is common to methods that rely on discretization of the entire domain (e.g., finite element limit analysis (Kong, 2015)) as well as the proposed method.

5. Simulation of smooth wedge indentation and ploughing

The performance of the proposed SKM model is first examined in the case of indenting and ploughing a Tresca solid by a smooth rigid wedge (i.e., the interface strength $c_a = 0$). In this example, the wedge angle α (see Fig. 3 for its definition) equals to 10°, while the material cohesion $c = 13$ MPa. In the simulations, the

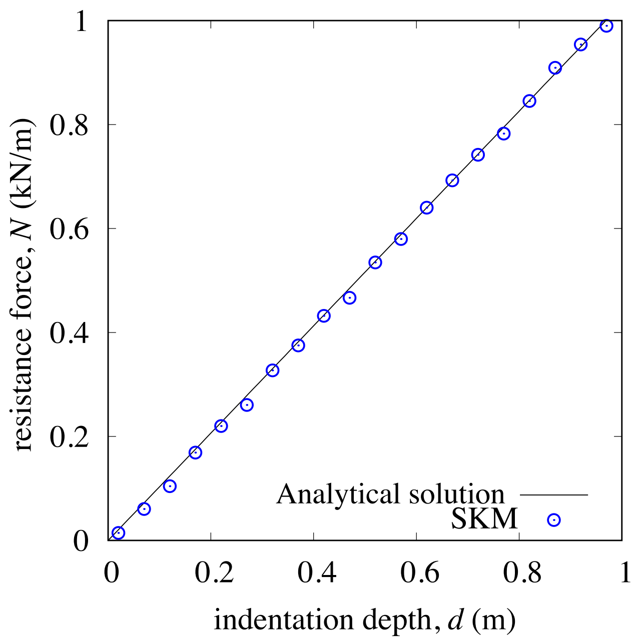

Fig. 8. Comparison between the penetration resistance computed by the SKM and slip-line solution (Hill et al., 1947). Note that the SKM simulation employs nodal spacing $\Delta x = 0.5$ and time increment $\Delta T = 0.05$.

wedge is first pushed into the plastic solid, followed by a lateral ploughing with the normal load maintained at the same level as the one reached at the end of the indentation. Both indentation and ploughing processes are under displacement control in the simulations (i.e., the velocity v_x or v_y in Fig. 3(a) is prescribed).

Fig. 8 compares the computed indentation resistance with that given by Hill et al. (1947)'s slip-line solution. A good agreement can be observed. Fig. 9 presents the optimal velocity fields (i.e., deformation mechanisms) when the intruder penetrates to different depths. These fields exhibit geometrically self-similarity, which is explicitly assumed in Hill et al. (1947)'s solution but comes out automatically from the SKM.

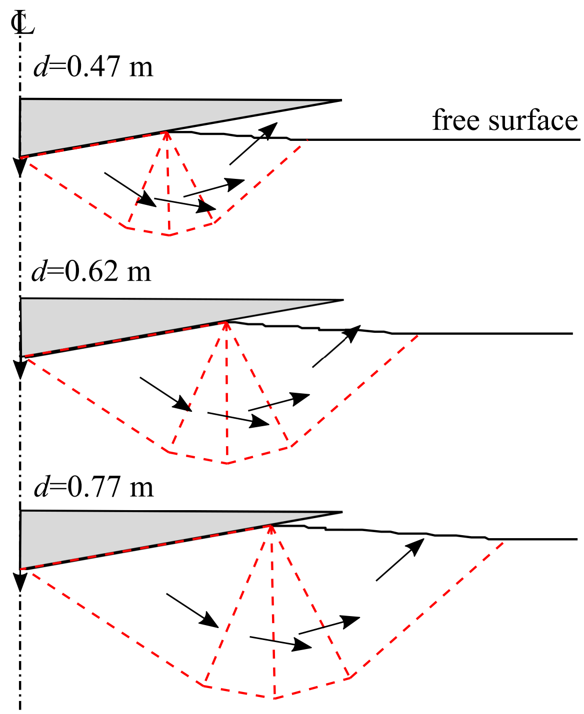

Fig. 9. SKM computed velocity field at various stages of rigid wedge indentation.

Fig. 10 shows the computed trajectory of the wedge as well as the normalized tangential force during the ploughing stage. The deformation mechanisms for selected instances are given in Fig. 11. It is seen that the initial lateral ploughing leads to a sinking of the wedge. This deformation pattern, referred to as "junction growth" within tribology (Tabor, 1959; Challen and Oxley, 1979), occurs because the contact pressure on the rear flank is relieved and the wedge penetrates deeper into the plastic solid to achieve a larger contact area at the front flank to sustain the applied normal load. As the lateral ploughing continues, the wedge begins to rise and simultaneously push a bow wave of plastically deformed material ahead as depicted in Fig. 11(b) and (d). Such rising phase continues until reaching a steady state characterized by approximately constant ploughing resistance and

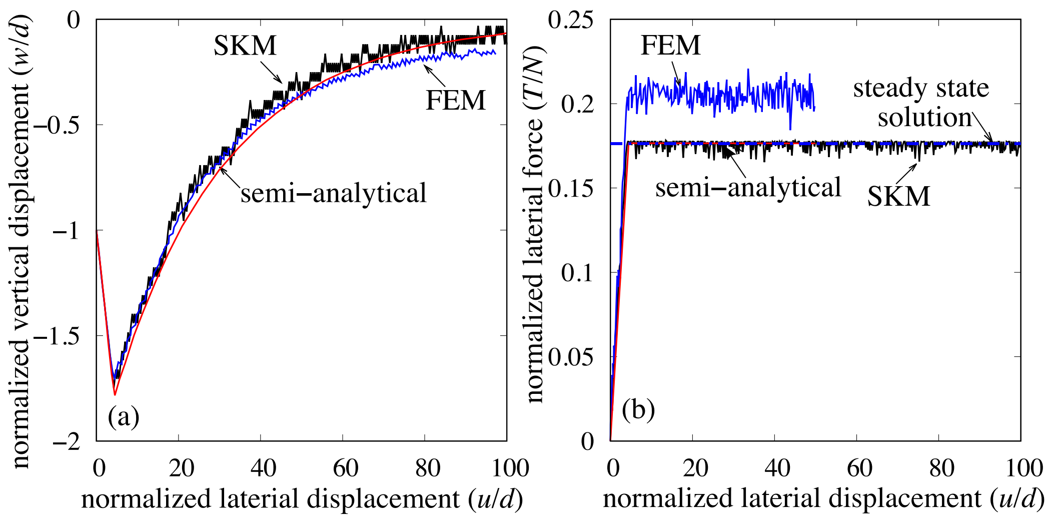

Fig. 10. Comparison between smooth wedge ploughing response computed by the SKM, finite element, semi-analytical method (Hambleton, 2010), and analytical steady-state solution (Challen and Oxley, 1979). Note that the SKM simulation employs nodal spacing $\Delta x = 1$ and time increment $\Delta T = 0.25$.

wedge vertical location. It is seen that the computed rising trajectory is not smooth but with small-amplitude oscillations. The latter is attributed to the alternation between two deformation mechanisms respectively depicted in Fig. 11(c) and (d). The former mode is characterized by the wedge sliding along its front flank without deforming the solid, which gradually reduces the contact area between the wedge and the solid mass. When the contact area is not enough to sustain the applied normal load, the second mode characterized by a bear-capacity type failure occurs. The contact area grows consequently.

To examine the accuracy of the SKM simulation, two alternative solutions are included in Fig. 10. Hambleton (2010) proposes a semi-analytical method by treating the ploughing as a sequence of incipient plastic flow problems that can be approximated by Hill et al. (1947)'s indentation mechanism. An FEM

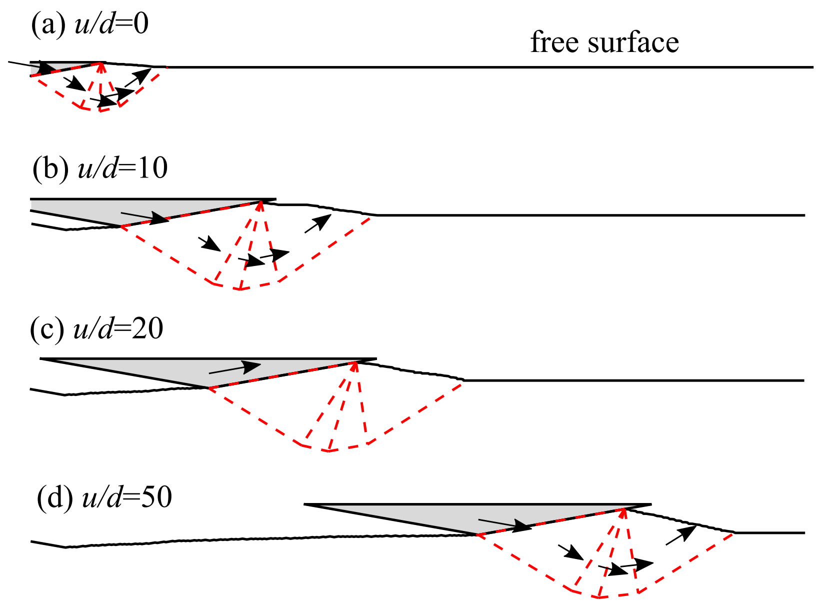

Fig. 11. SKM computed evolution of the material free surface and velocity fields during smooth wedge ploughing.

simulation is also performed by Hambleton (2010) to verify the semi-analytical model. This numerical analysis is conducted by using ABAQUS/Explicit. The arbitrary Lagrange-Eulerian (ALE) remeshing algorithm is employed in the region near the wedge to maintain a high-quality mesh after relatively large deformation has occurred. The rigid-plastic behavior of the solid is emulated by using the Tresca model with a large value of Young's modulus E (e.g., $E/c \approx 7000$). More detailed discussions on the features of the FEM can be found in Hambleton and Drescher (2012, 2009). A good agreement can be seen from these comparisons. The steady-state ploughing forces computed by the SKM and semi-analytical approach are very close to the one obtained by slip-line technique (Challen and Oxley, 1979), while the FEM tends to predict a bit higher resistance. Note that the FEM simulation shows similarly oscillatory wedge trajectory and ploughing resistance, as computed by the SKM.

6. Convergence analysis of SKM simulation

We use the ploughing simulation discussed in the previous section as an opportunity to evaluate the convergence features of the SKM solution with respect to the discretization size of the free surface represented by the nodal space, Δx, and the step size of the time marching represented by the time increment, ΔT.

Fig. 12(a) and (b) shows the ploughing simulations performed under three different time steps. It can be seen that the computed wedge trajectory and tangential force both show a converging tendency as ΔT decreases. The decrease in the time step also leads to smaller fluctuations in the computed response. The same convergence feature can be observed for reducing the nodal spacing Δx, as illustrated in Fig. 12(c) and (d). It is noticed that the simulations based on larger nodal spaces generate trajectories that elevate to higher positions. Such response might result from the fact that a linear function is used to interpolate the free surface between adjacent nodes (see the inset of Fig. 12(c)). In this illustration, the solid and dashed lines represent the free surface before and after the update, and the gray area denotes the factitious material that is added to preserve the continuity of the free surface. Larger nodal space implies more artificial material is piled up ahead of the wedge and consequently the deformation mode associated with wedge upward motion (e.g., that shown in Fig. 11(c)) can be sustained for longer periods. As a consequence, the wedge heads to larger elevations.

The aforementioned analyses indicate that the volume conservation for incompressible Tresca solid can be violated in SKM simulations, due to the resources like the addition of artificial material mentioned above and the correction of the

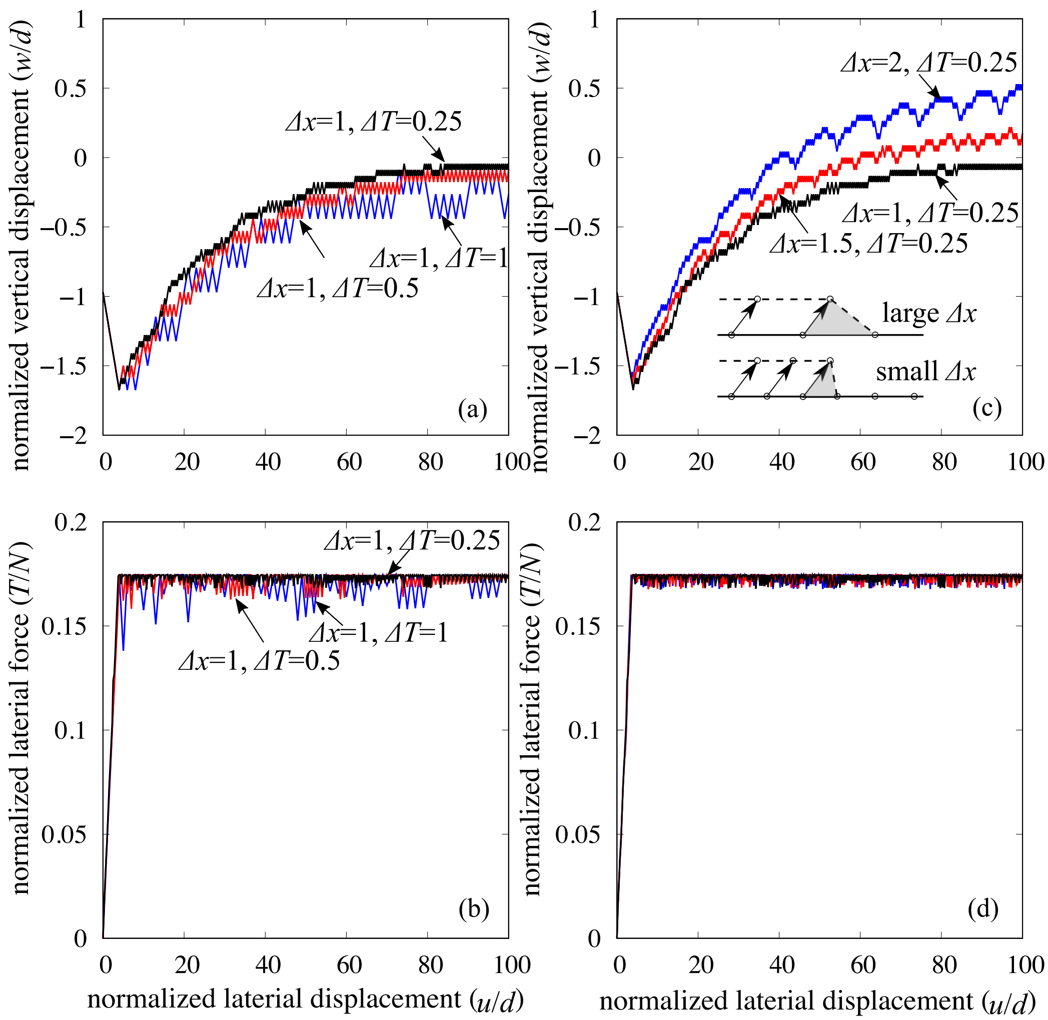

Fig. 12. Convergence analyses of SKM solution with respect to time increment size (subfigures (a) and (b)) and nodal space along the discretized free surface (subfigures (c) and (d)).

material free surface discussed in section 4. To assess how this violation is affected by the employed nodal spacing and time increment, the change of material volume in the convergence analysis is evaluated (see Table 1). These reported volume changes are computed by numerically integrating the material free surface at the end of the simulations. The data suggest that the change of material volume tends

Table 1. Change of material volume at the end of ploughing simulations that employ different nodal spacing and time increment (see Fig. 12). Note that the volume change is normalized by the initial volume before ploughing, V_0. This initial volume corresponds to a rectangular region with a depth twice the wedge indentation depth prior to ploghing d and a length twice the lateral ploughing distance u, i.e., $V_0 = 4du$.

Nodal spacing, Δx	Time increment, ΔT	Change of material volume, $\Delta V/V_0$
1.0	1.0	-7.6 %
1.0	0.5	-3.6 %
1.0	0.25	-2.0 %
1.5	0.25	-1.1 %
2.0	0.25	0.01 %

to decrease as smaller time increments are employed (i.e., compare lines 1 to 3 of Table 1). On the other hand, when larger nodal spacing is used, more artificial material can be added to computation domain (i.e., compare lines 3 to 5 of Table 1), as discussed above.

7. Simulation of rough wedge indentation and ploughing

We have shown that the r-adaptive SKM model can reasonably represent the deformation processes of a Tresca solid ploughed by a smooth wedge. In this section, we further evaluate this technique in the case of ploughing cohesive solid by wedge where finite adhesion presents at contact surfaces. The experimental observations for ploughing aluminum alloy by a hard wedge (Challen et al., 1984) are used to assess the model. These tests are chosen become they provide a rich dataset (e.g., the evolution of ploughing resistance and tool trajectory) that helps to evaluate the SKM model relatively comprehensively. Albeit being different materials, the mechanical behavior of metal and cohesive soil (e.g., undrained clay) is similar in some key aspects such as incompressibility conditions. Due to this reason, constitutive models and analytical solutions developed originally for metal have been successfully employed to analyze geotechnical problems (Mroz, 1967; Prévost, 1977; Lemaitre and Chaboche, 1990; Anastasopoulos et al., 2011; Karapiperis and Gerolymos, 2014; Prandtl, 1920; Terzaghi, 1943). Following this line of thought, simulating the tests of ploughing metal is expected to provide a meaningful evaluation of the SKM model regarding its capacity to model the counterpart geotechnics problems (e.g., ploughing cohesive soil (Hettiaratchi and Reece, 1974; Palmer, 1999; Atkins, 2009) and the lateral sliding of pipeline in undrained clay (Tian and Cassidy, 2010; White and Dingle, 2011)).

Table 2 summarizes the geometric and material parameters used in the simulations. The material properties are reported by Challen et al. (1984) except that for the test 12, which is not available from the literature. This information is estimated in this study by fitting the steady-state ploughing force. In the simulations, an indentation stage is modeled prior to the ploughing, which ceases when the normal forces applied in the experiments (see Table 2) are reached. Due to the lack of experimental data, a comparison between the computed and measured evolution of the penetration resistance with the indentation depth is not available. Nevertheless, the comparison between the calculated and measured wedge tip elevation at the beginning of the ploughing (see Figs. 13, 14 and 15) suggests that the indentation stage is reasonably represented by the model.

Comparisons of full force-displacement histories for the three ploughing tests are shown in Figs. 13, 14 and 15. In general, a good agreement can be seen be-

Table 2. Parameters in the SKM simulations of the ploughing tests performed by Challen et al. (1984).

Test	α (°)	N (N/mm)	c (MPa)	c_a (MPa)
10	25.9	700	243	26.73
12	35.05	700	200	30
19	10.2	700	193	82.99

tween the computed and observed response. The calculated steady-state ploughing forces and velocity fields (see Fig. 16) also match reasonably with the slip-line solution proposed by Challen and Oxley (1979). However, quantitative mismatches between model simulations and test data can also be observed. For example, the simulations show that there is a sudden drop of tangential force once the wedge starts to rise (see Fig. 14), resulting from the separation at the rear flank of the wedge and the consequent loss of resistance related to the interface strength. This feature is not observed from test results, where the separation may be a progressive process and thus leading to a smooth change of the ploughing resistance. Remarkable hardening and softening stages are observed from the experimental data of test 19, which are not captured by the model possibly due to the underlying assumption that the solid is perfectly plastic. Furthermore, it is observed that the computed steady-state resistance by the SKM coincides with the analytical solution given by Challen and Oxley (1979) for the test 10 (see Fig. 13), whereas those computed for the tests 19 and 12 are reasonably close to yet not exactly the same as the analytical solution (see Figs. 14 and 15). This difference might result from the variation in SKM performance between different cases. In simulating Challen et al. (1984)'s tests, efforts are made to ensure a consistency regarding modeling

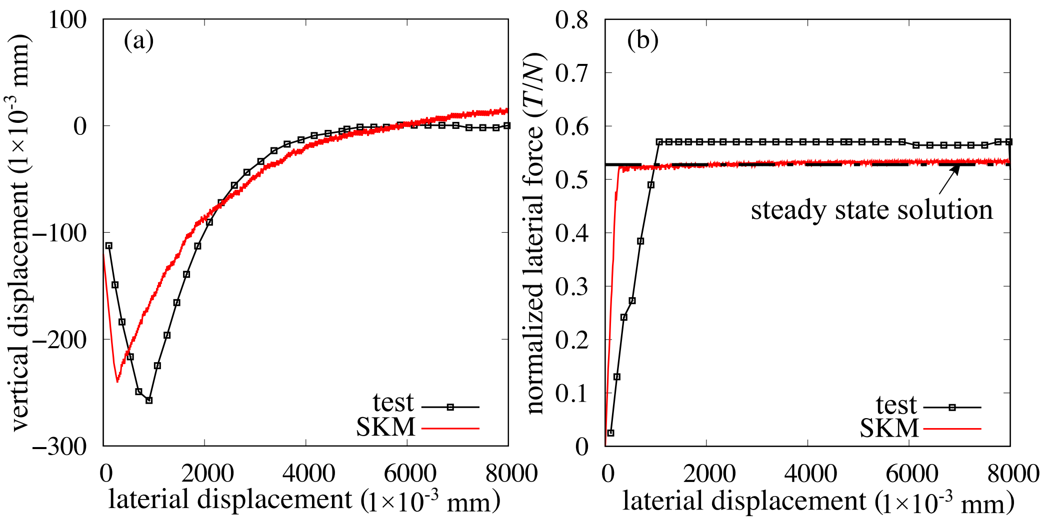

Fig. 13. Comparison between SKM simulated ploughing response, experimental data (test 10 in Challen et al. (1984)) and analytical steady-state solution (Challen and Oxley, 1979). Note that the SKM simulation employs nodal spacing $\Delta x = 60$ and time increment $\Delta T = 10$.

settings, e.g., nodal spacing and time increment (see the caption of Figs. 13 to 15). Nevertheless, the accuracy of the SKM simulations might still vary between different cases, possibly due to that material properties vary across these tests (see Table 2).

The computation times (total runtime) and the number of Mosek calls for the simulations described above are summarized in Table 3. It is seen that the cost of using r-adaptive SKM for simulating large deformation processes is relatively small. The runtime can potentially be brought down further via the implementation of Mosek through platforms that require smaller overhead than Matlab. The fact that the simulation of the test 12 consumes the largest cost is because a smaller value of the parameter T_s (see section 3.2 for its definition) is employed to ensure the solution accuracy and consequently more iterations are conducted in the non-linear optimization of Eq. (7).

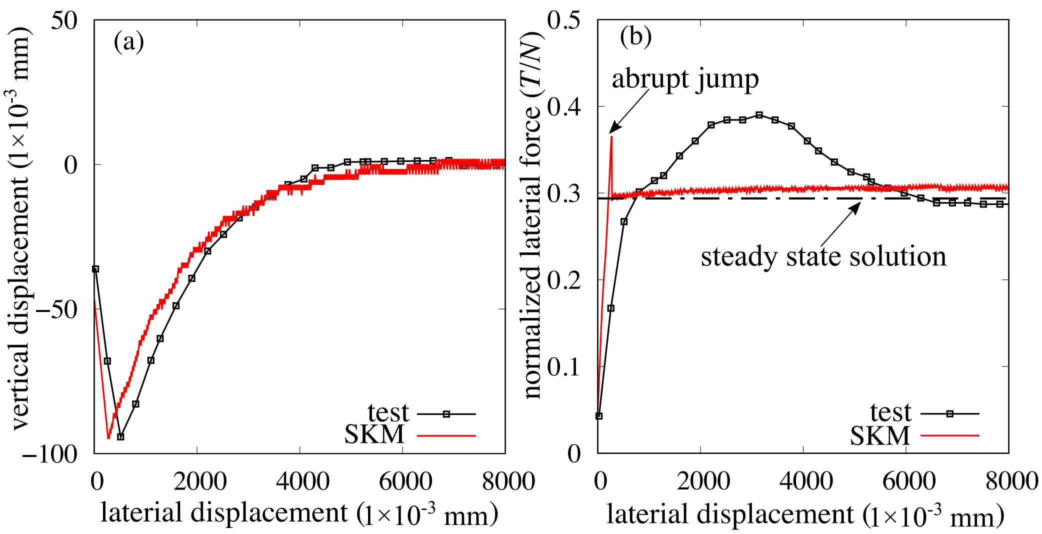

Fig. 14. Comparison between SKM simulated ploughing response, experimental data (test 19 in Challen et al. (1984)) and analytical steady-state solution (Challen and Oxley, 1979). Note that the SKM simulation employs nodal spacing $\Delta x = 60$ and time increment $\Delta T = 10$.

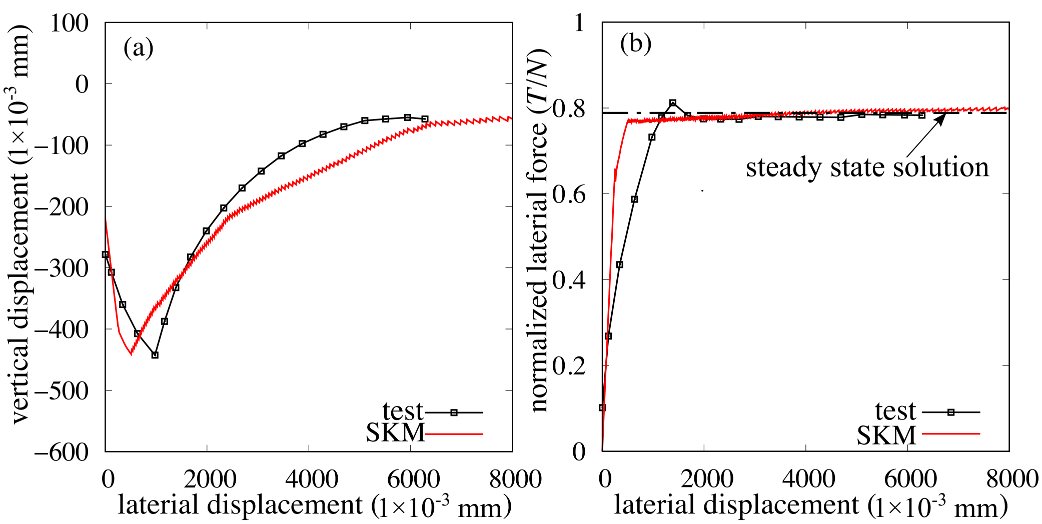

Fig. 15. Comparison between SKM simulated ploughing response, experimental data (test 12 in Challen et al. (1984)) and analytical steady-state solution (Challen and Oxley, 1979). Note that the SKM simulation employs nodal spacing $\Delta x = 60$ and time increment $\Delta T = 10$.

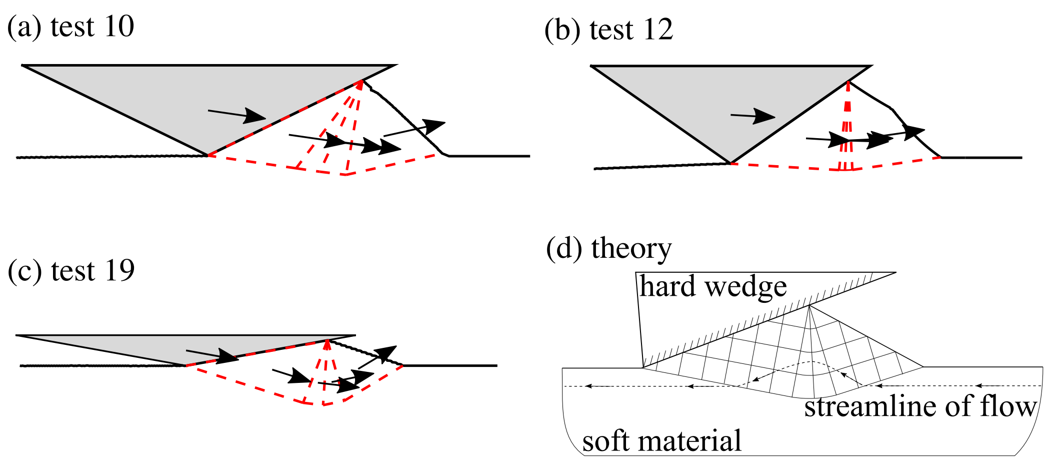

Fig. 16. Comparison between SKM computed steady-state velocity fields and that postulated in slip-line solution (reproduced from Challen and Oxley (1979)).

8. Simulation of cylinder penetration in undrained clay

To illustrate the application of the proposed SKM to other evolutionary plasticity problems in geotechnical engineering, plain-strain cylinder penetrating undrained clay is simulated in the following. As previously mentioned, this deformation process is similar to that taking place during the T-bar penetrometer test in geotechnical

Table 3. Computation times (unit:second) and Mosek calls for SKM simulations of lateral ploughing. Note that the reported times are total runtime on a PC equipped with an Intel i9-9900 processor (3.6 GHz; 8 cores) and 32 GB RAM. Test numbers in the table refer to those performed by Challen et al. (1984).

Cases	Total runtime	Number of Mosek calls
Test 10	251	19624
Test 12	900	97071
Test 19	241	23545

site characterization (Einav and Randolph, 2005).

Figure 17 shows the kinematic mechanism used in the SKM simulations. Considering the symmetry of the problem, only half of the domain is modeled. The T-bar penetrometer is approximated by a rigid polygon (see Fig. 17(a)) that allows treating the soil-tool interface as planar velocity discontinuities. The SKM progressively adds new blocks to kinematic mechanism to facilitate the growth in the contact region between soils and T-bar during its penetration. Specifically, a new pair of rigid blocks are included (see Fig. 17(b)) when a new polygon edge becomes in contact with the soil free surface (e.g., BC in Fig. 17(b)). To ease the comparison between the SKM simulations and existing solutions, we consider that the shear strength of undrained clay S_u distributes uniformly along depths. The Tresca solid is used to approximate undrained clay, i.e., cohesion c in Eq. (1) equals to S_u. The soil-tool interface is considered to be rough and feature strength $c_a = S_u/2$. The simulation is performed by prescribing the velocity of the T-bar (i.e., v_y in Fig. 17). Other model settings are the same as those employed in the aforementioned wedge ploughing example.

Figure 18 show the computed variation of penetration resistance with depths by the SKM and finite element method (FEM) (Zhu et al., 2020). In the FEM simulation, Coupled Eulerian-Lagrangian (CEL) technique is used to handle the large deformation of soil, while the Tresca model is used to describe the behavior of undrained clay. More detailed discussions on the features of the FEM modeling can be found from Kong (2015), Kong et al. (2018), and Zhu et al. (2020). The results given by the two numerical approaches agree reasonably, and show a consistent trend that the penetration resistance grows at smaller rates as the depth increases. The analytical solutions proposed by Hambleton and Drescher (2012)

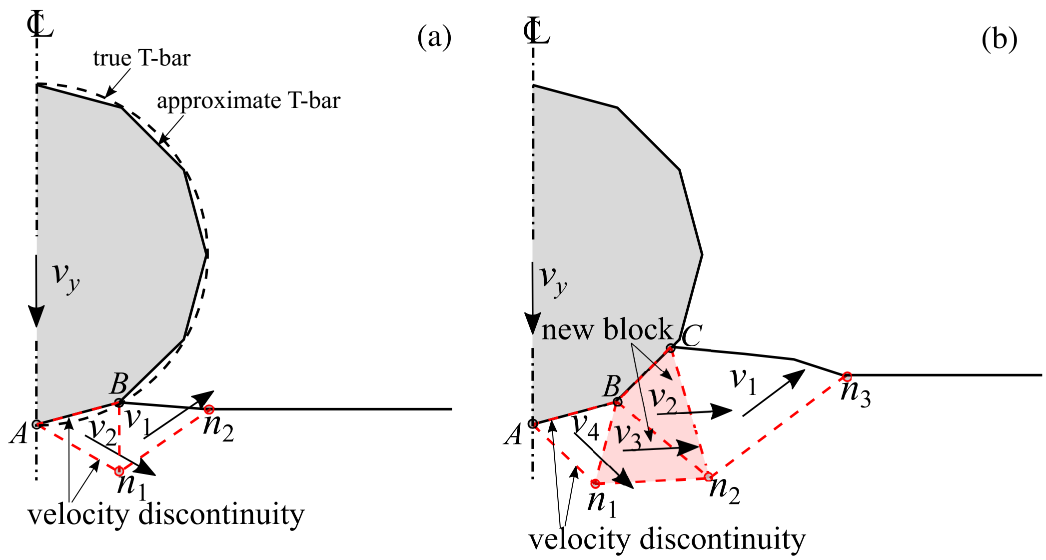

Fig. 17. Kinematic mechanism in the simulation of rigid cylinder penetration: (a) early contact; (b) new blocks are added to facilitate the growth in soil-tool contact area.

and Einav and Randolph (2005), applicable respectively to shallow and deep T-bar penetration, are included in Fig. 18. In the former work, a closed-form solution for cylinder indentation is constructed by examining asymptotic state of evolutionary processes characterized by the Prandtl-type punch mechanism (Hambleton and Drescher, 2012). The latter study presents a upper bound solution for a cylindrical plane-strain object translating through a rigid plastic solid (Einav and Randolph, 2005). Figure 18 shows that the force-penetration relationship computed by the SKM matches reasonably with the solution of Hambleton and Drescher (2012) at shallow depths, while approaches to the solution of Einav and Randolph (2005) at deep locations.

The change in the free surface and deformation mechanism of soil as the penetration proceeds is presented in Fig. 19. These patterns of evolving material geometries are consistent with those revealed from FEM simulations (Kong et al.,

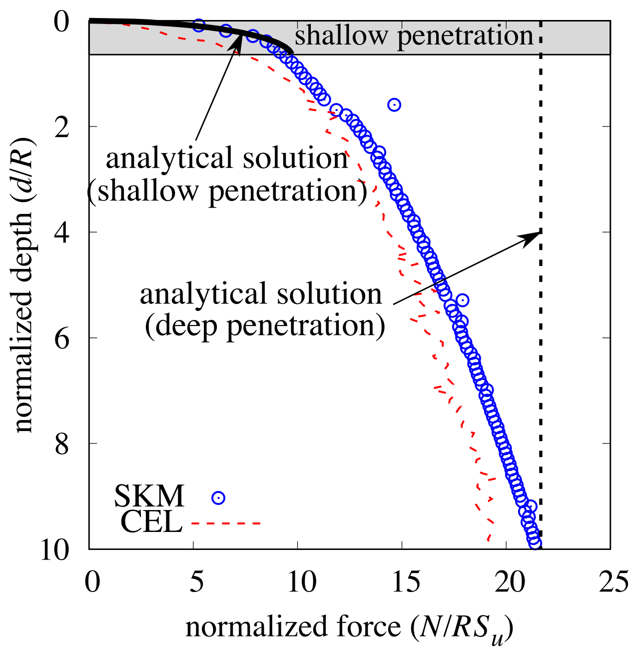

Fig. 18. Force-displacement relationship during cylinder penetration process computed by the SKM, Coupled Eulerian-Lagrangian (CEL) finite element method, and analytical models. Note that the SKM simulation employs nodal spacing $\Delta x = 0.01$ and time increment $\Delta T = 0.02$. The analytical solution for shallow penetration is described in Hambleton and Drescher (2012), while that for deep penetration is given by Einav and Randolph (2005).

2017; Zhu et al., 2020), except that the SKM computes global flow deformation mechanism for deep penetration (albeit that the magnitude of soil velocities at shallow depths is noticeably reduced, see Fig. 19(c)), rather than local full-flow mechanism as seen in the upper bound solution of Einav and Randolph (2005). The reasons behind such discrepancy will be discussed in the following section.

9. Possibilities and limitations of SKM

We have shown that how two archetypal problems of evolutionary plasticity processes (wedge ploughing and cylinder penetration) can be modeled by the SKM

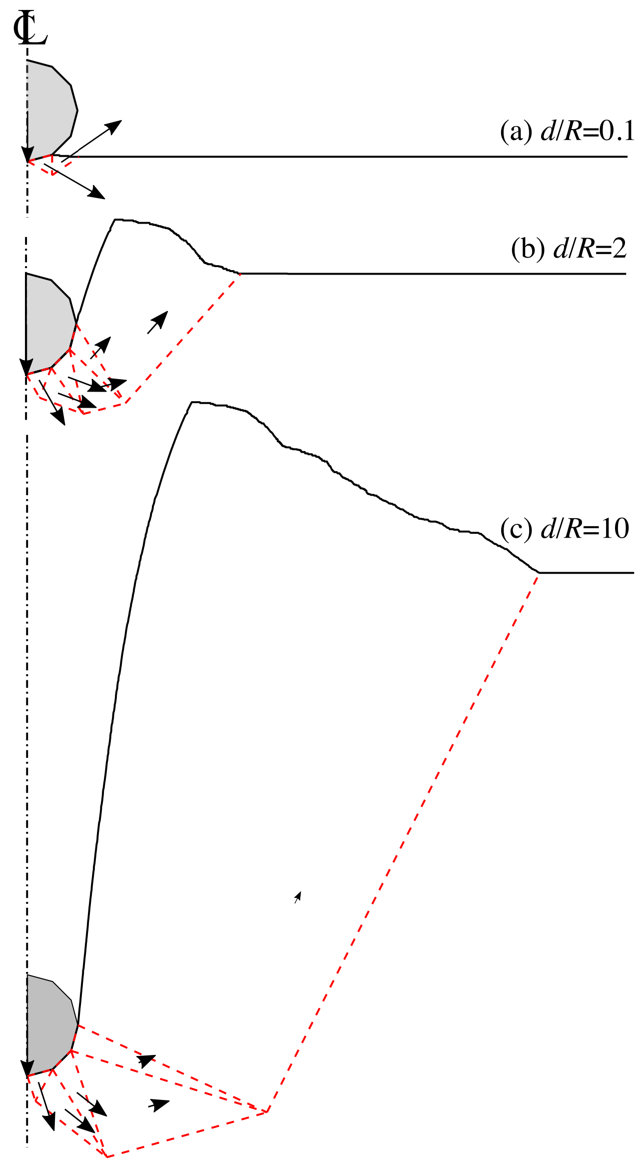

Fig. 19. Material free surface and soil deformation mechanism computed by the SKM that correspond to different cylinder penetration depths.

in combination with simple kinematic mechanism. By comparing against analytical and numerical solutions as well as experimental evidence in the literature, we show that the SKM can reasonably evaluate the first-order response of the problem (i.e., the force-displacement history and tool trajectories). The key behind this modeling success is to captures the evolution of material geometries (e.g., free surface) due to the large deformation.

The present study has been focused on the evolutionary plasticity processes involving Tresca solid (cohesive soil). This cohesive material is selected to simplify the problems such that the key characteristics of the fundamental concept of simulating large deformation processes via SKM can be explored. Specifically, given the incompressibility conditions of cohesive material, the dilation at velocity discontinuities and the consequent potential material separation or overlay taking place during geometry update can be avoided. On the other hand, it should be noted that the SKM strategy can be applied to the problems dealing with frictional materials, as demonstrated by modeling thrusting sequences in geology (Cubas et al., 2008; Mary et al., 2013) and ploughing sand (Hambleton et al., 2014; Kashizadeh et al., 2015). In these studies, the dilatancy of cohesionless materials at velocity discontinuities is often neglected when the material geometry is incrementally updated, as a means to avoid the aforementioned complications. Therefore, when extending the proposed SKM method to frictional materials, future investigations are needed on the methods to update the material geometries in accordance with deformation mechanisms featuring finite dilatancy at velocity jumps.

The proposed SKM formulation characterizes material deformation patterns by the simple mechanism of rigid elements. This modeling decision reduces the number of unknowns required to constrain an optimal kinematic field and consequently leads to relatively efficient simulations. Nevertheless, it should be

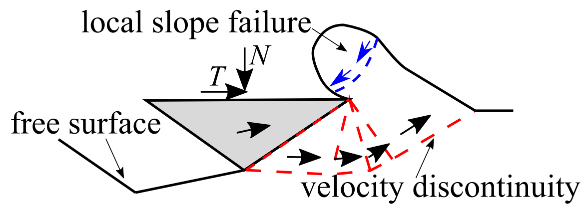

Fig. 20. Schematic illustrating the conditions of overtopping, where material deformation characteristics such as local slope failure cannot be represented by rigid element mechanism.

noted that there are cases where the aforementioned simple mechanism is not sufficient to characterize material deformation patterns. For instance, when a wedge with finite size keep ploughing Tresca solid, the cohesive material at some times might start to overtop the moving object, as shown in Fig. 20. Under these conditions, the material deformation can feature characteristics that cannot be represented by simple kinematic mechanism, like local slope failure.

To accommodate these deformation patterns, the current SKM model needs to employ more sophisticated kinematic mechanisms such as deformable elements and the deformation of the material not immediately adjacent to the object. For this purpose, the energy dissipation due to the deformation of elements needs to be included in the *r*-adaptive kinematic method, while broader material domain requires to be discretized by mesh (see Kong (2015) for a detailed discussion on formulating SKM based on finite element limit analysis). On the other hand, it should be noted that, while more sophisticated mechanisms can more accurately capture the material deformation, they inevitably increase computation cost. Therefore, the selection of kinematic mechanism in the SKM depends on "cost/benefit" considerations done for specific engineering projects.

The response computed by the proposed SKM model strongly relies on the algorithms used to search for an optimal velocity field (i.e., the algorithms used to solve the non-linear optimization of Eq. (7)). Local optimization algorithm is currently employed due to that it is generally more efficient than its global optimization counterparts. Nevertheless, this type of algorithm might return local optimum and the kinematic mechanism that is not the most critical. As mentioned above, global deformation pattern is computed by the SKM when the cylinder has been pushed to relatively deep depths (see Fig. 21(a)). In fact, local deformation pattern can correspond to smaller resistance (see the N/RS_u values depicted in Fig. 21(a) and (b)) and thus representing a more critical mechanism. This alternative mechanism can be computed from the current formulation when the optimization solver starts with different initial guesses of nodal positions. Continuous investigations are required to explore the possibility of resolving this dependence on initial nodal positions without sacrificing computational efficiency, like via global surrogate optimization.

In addition to initial nodal positions, the performance of the optimization solver can be sensitive to its controlling parameters, so does the response computed by the SKM model. We use the test 12 performed by Challen et al. (1984) to illustrate this point. It is seen from Fig. 22 that employing a higher value for the parameter T_s (i.e., stop the optimization prematurely) only marginally overestimates the ploughing force over the first half of the deformation process, but leading to remarkable changes in the computed wedge trajectories and material free surface. The cumulative changes in the geometric configurations eventually reach a breakpoint (i.e., the square symbol in Fig. 22) where the deformation mode fundamentally changes (see the inset of Fig. 22), so does the corresponding ploughing resistance. Future studies can explore the possibility of regularizing the aforementioned dependence of solution on optimization solver parameters

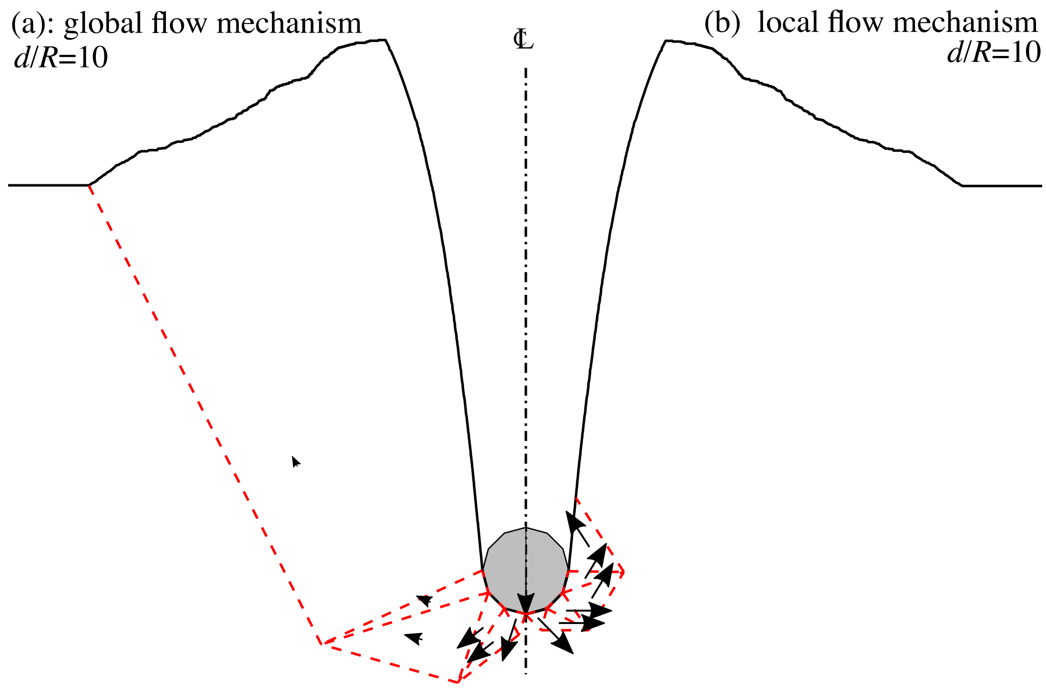

Fig. 21. Deformation mechanism for deep penetration of cylinder.

via including deformable elements in kinematic mechanism, as the rigid block assumption might pose overly strong restrictions on available deformation modes.

The last limitation of the SKM model observed in the present study is that the solution can be sensitive to the presence of irregular shape along the material free surface and thus requiring careful correction of the surface. To illustrate this point, Fig. 23 shows the effects of permitting the sharp inverse corner at the free surface. Similar to relaxing the optimization tolerance described above, the irregular shape of the free surface can promote remarkable changes on the computed deformation mode and peculiar jumps in the ploughing forces. This is because the boundary between the moving and stationary materials is trapped at the tip of the inverse angle (see the computed velocity fields in Fig. 23). The issue mentioned above can

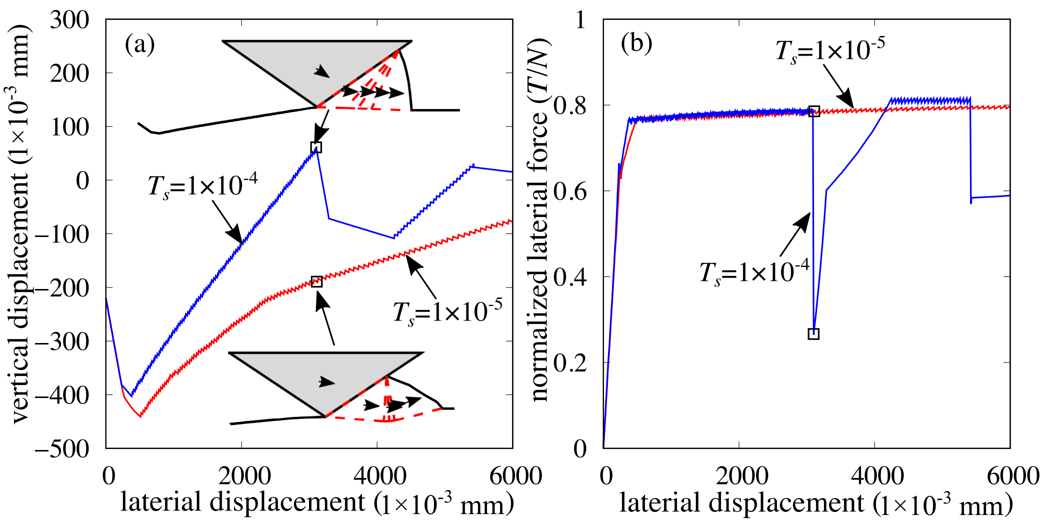

Fig. 22. Influence of the non-linear optimization tolerance T_s on the computed ploughing response.

be addressed by the surface correction scheme discussed in Section 4. However, it should be noted that these correction strategies can violate the conservation of mass, as materials are deleted (for correcting penetration) or added (for correcting the inverse corner). Such induced error can be minimized as relatively small time increments are adopted (see Table 1).

10. Conclusions

This work investigates the potentials of simulating evolutionary plasticity processes via sequential kinematic method (SKM) constructed on simple deformation mechanism. These processes are modeled by sequentially updating the material geometries in accordance with velocity fields represented by mechanism consisting of rigid translational elements separated by velocity discontinuities. Optimal velocity fields are sought by a r-adaptive kinematic method formulation, where an iterative, nested optimization procedure is constructed that consists of (1) de-

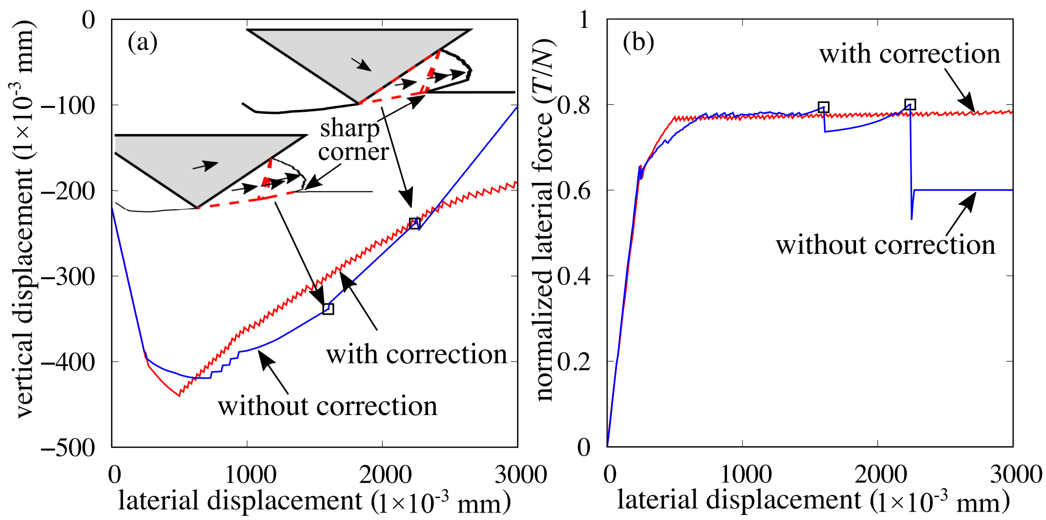

Fig. 23. Influence of the free surface correction on the computed ploughing response.

termination of velocities for a fixed mesh of rigid blocks using second-order cone programming and (2) adaptation of nodal positions using non-linear optimization to find a critical layout of velocity discontinuities. The advantages and limitations of the modeling strategy are examined through simulating wedge ploughing Tresca solid and cylinder penetrating undrained clay, where analytical, numerical solutions and experimental observations are available in the literature. The main conclusions can be drawn from this work include:

1. The comparison of the results simulated by using the proposed SKM model against existing solutions and experimental evidence shows that SKM combined with conceptually simple deformation mechanism can reasonably represent the first-order response of wedge ploughing and cylinder penetration, including forces and motions of the object.
2. The proposed SKM technique exhibits promising features for delivering efficient analyses of evolutionary plasticity problems.

3. The response computed by the SKM depends on spatial and temporal discretization sizes. A converging trend of simulations is seen as the nodal space of the discretized free surface or time increment size become smaller.
4. Both employing a sufficiently small termination tolerance for the non-linear optimization of the nodal positions and appropriately correcting the material free surface can be crucial for obtaining accurate simulations. Without these restrictions, a significant deviation on the objects' trajectories and the material free surface can occur without noticeably altering the computed forces. However, the accumulation of errors in the geometries can eventually lead to large mismatches on the prediction of resistance.
5. The employed local optimization solver can return kinematic mechanism that is not the most critical, depending on the initial guesses of nodal positions.

In future studies, the proposed SKM model can be extended to the problems dealing with frictional materials. In this aspect, more research efforts might be required focusing on the methods for updating material geometries that can accommodate finite dilation at velocity discontinuities. The dependence of kinematic mechanism optimization on initial nodal positions might be resolved by employing efficient global optimization solvers (e.g., surrogate model). The proposed SKM model applies most appropriately if the engineering interest is to quickly evaluate large-deformation plasticity problems to the first order. When the primary interests rest on more accurate representations of soil deformation or detailed response such as the stress and strain fields, the current formulation can be augmented by more sophisticated kinematic mechanisms (e.g., Kong (2015), Kong et al. (2018), Zhu et al. (2020)), or modeling techniques other than SKM can be pursued (e.g., Agarwal et al. (2019), Afrasiabi et al. (2019) and Recuero et al. (2017)).

Acknowledgements

This material is based upon work supported by the National Science Foundation under Grant No. 1846817. This financial support is gratefully acknowledged. The first and second authors acknowledge support provided by the National Natural Science Foundation of China under Grant Nos. 51738010 and 41902278.

References

Afrasiabi, M., Roethlin, M., Klippel, H., Wegener, K., 2019. Meshfree simulation of metal cutting: an updated Lagrangian approach with dynamic refinement. International Journal of Mechanical Sciences 160, 451–466. doi:10.1016/j.ijmecsci.2019.06.045.

Agarwal, S., Senatore, C., Zhang, T., Kingsbury, M., Iagnemma, K., Goldman, D.I., Kamrin, K., 2019. Modeling of the interaction of rigid wheels with dry granular media. Journal of Terramechanics 85, 1–14. doi:10.1016/j.jterra.2019.06.001.

Anastasopoulos, I., Gelagoti, F., Kourkoulis, R., Gazetas, G., 2011. Simplified constitutive model for simulation of cyclic response of shallow foundations: Validation against laboratory tests. Journal of Geotechnical and Geoenvironmental Engineering 137, 1154–1168.

Atkins, T., 2009. The Science and Engineering of Cutting-The Mechanics and Processes of Separating, Scratching and Puncturing Biomaterials, Metals, and Non-metals. Butterworth Heinemann, Oxford, England. doi:10.1016/C2009-0-17178-7.

Bil, H., Kiliç, S.E., Tekkaya, A.E., 2004. A comparison of orthogonal cutting data from experiments with three different finite element models. International Journal of Machine Tools and Manufacture 44, 933–944. doi:10.1016/j.ijmachtools.2004.01.016.

Challen, J.M., McLean, L.J., Oxley, P.L.B., 1984. Plastic deformation of a metal surface in sliding contact with a hard wedge: Its relation to friction and wear. Proceedings of the Royal Society A: Mathematical, Physical and Engineering Sciences 394, 161–181. doi:10.1098/rspa.1984.0074.

Challen, J.M., Oxley, P.L., 1979. An explanation of the different regimes of friction and wear using asperity deformation models. Wear 53, 229–243. doi:10.1016/0043-1648(79)90080-2.

Chen, W.F., 1975. Limit Analysis and Soil Plasticity. Elsevier Scientific Publishing Company, Amsterdam, The Netherlands.

Collins, I.F., 1972. A simplified analysis of the rolling of a cylinder on a rigid/perfectly plastic half-space. International Journal of Mechanical Sciences 14, 1–14. doi:10.1016/0020-7403(72)90002-1.

Corradi, L., Panzeri, N., 2004. A triangular finite element for sequential limit analysis of shells. Advances in Engineering Software 35, 633–643. doi:10.1016/j.advengsoft.2004.03.014.

Cubas, N., Leroy, Y.M., Maillot, B., 2008. Prediction of thrusting sequences in accretionary wedges. Journal of Geophysical Research: Solid Earth 113, B12412. doi:10.1029/2008JB005717.

Dayal, U., Allen, J.H., 1975. The effect of penetration rate on the strength of remolded clay and sand samples. Canadian Geotechnical Journal 12, 336–348.

De Vathaire, M., Delamare, F., Felder, E., 1981. An upper bound model of ploughing by a pyramidal indenter. Wear 66, 55–64. doi:10.1016/0043-1648(81)90032-6.

Drucker, D.C., Prager, W., Greenberg, H.J., 1952. Extended limit design theorems for continuous media. Quarterly of Applied Mathematics 9, 381–389. doi:10.1090/qam/45573.

Ducobu, F., Rivière-Lorphèvre, E., Filippi, E., 2016. Application of the Coupled Eulerian-Lagrangian (CEL) method to the modeling of orthogonal cutting. European Journal of Mechanics, A/Solids 59, 58–66. doi:10.1016/j.euromechsol.2016.03.008.

Einav, I., Randolph, M.F., 2005. Combining upper bound and strain path methods for evaluating penetration resistance. International Journal for Numerical Methods in Engineering 63, 1991–2016.

Godwin, R.J., O'Dogherty, M.J., 2007. Integrated soil tillage force prediction models. Journal of Terramechanics 44, 3–14.

Hambleton, J.P., 2010. Plastic analysis of processes involving material-object interaction. Ph.D. thesis. The University of Minesota. Minneapolis and Saint Paul, United States.

Hambleton, J.P., Drescher, A., 2009. On modeling a rolling wheel in the presence of plastic deformation as a three- or two-dimensional process. International

Journal of Mechanical Sciences 51, 846–855. doi:10.1016/j.ijmecsci.2009.09.024.

Hambleton, J.P., Drescher, A., 2012. Approximate model for blunt objects indenting cohesive-frictional materials. International Journal for Numerical and Analytical Methods in Geomechanics 36, 249–271. doi:10.1002/nag.1004.

Hambleton, J.P., Sloan, S.W., 2013. A perturbation method for optimization of rigid block mechanisms in the kinematic method of limit analysis. Computers and Geotechnics 48, 260–271. doi:10.1016/j.compgeo.2012.07.012.

Hambleton, J.P., Stanier, S.A., White, D.J., Sloan, S.W., 2014. Modelling ploughing and cutting processes in soils. Australian Geomechanics 49, 147–156.

Herfelt, M.A., Krabbenhøft, J., Krabbenhøft, K., 2021. Modelling of 'no-tension' interfaces. Computers and Geotechnics 129, 103860.

Hettiaratchi, D., Reece, A., 1974. The calculation of passive soil resistance. Géotechnique 24, 289–310.

Hill, R., Lee, E., Tupper, S., 1947. The theory of wedge indentation of ductile materials. Proceedings of the Royal Society of London. Series A. Mathematical and Physical Sciences 188, 273–289. doi:10.1098/rspa.1947.0009.

Houlsby, G.T., Puzrin, A.M., 1999. The bearing capacity of a strip footing on clay under combined loading. Proceedings of the Royal Society of London. Series A: Mathematical, Physical and Engineering Sciences 455, 893–916.

Hryciw, R.D., Raschke, S.A., Ghalib, A.M., Horner, D.A., Peters, J.F., 1997. Video tracking for experimental validation of discrete element simulations of large discontinuous deformations. Computers and Geotechnics 21, 235–253. doi:10.1016/s0266-352x(97)00014-1.

Hwan, C.L., 1997. Plane strain extrusion by sequential limit analysis. International Journal of Mechanical Sciences 39, 807–817. doi:10.1016/s0020-7403(96)00089-6.

Johnson, D., 1995. Yield-line analysis by sequential linear programming. International Journal of Solids and Structures 32, 1395–1404. doi:10.1016/0020-7683(94)00200-G.

Karapiperis, K., Gerolymos, N., 2014. Combined loading of caisson foundations in cohesive soil: Finite element versus Winkler modeling. Computers and Geotechnics 56, 100–120.

Kashizadeh, E., 2017. Theoretical and Experimental Analysis of the Cutting Process in Sand. Master's thesis. The University of Newcastle. Callaghan, Australia.

Kashizadeh, E., Hambleton, J.P., Stanier, S.A., 2015. A numerical approach for modelling the ploughing process in sands, in: Analytical Methods in Petroleum Upstream Applications, CRC Press. pp. 159–164.

Kong, D., 2015. Large displacement numerical analysis of offshore pipe-soil interaction on clay. Ph.D. thesis. University of Oxford. Oxford, England.

Kong, D., Martin, C., Byrne, B., 2017. Modelling large plastic deformations of cohesive soils using sequential limit analysis. International Journal for Numerical and Analytical Methods in Geomechanics 41, 1781–1806.

Kong, D., Martin, C.M., Byrne, B.W., 2018. Sequential limit analysis of pipe–soil interaction during large-amplitude cyclic lateral displacements. Géotechnique 68, 64–75. doi:10.1680/jgeot.16.p.256.

Ladd, C.C., Foott, R., 1974. New design procedure for stability of soft clays. Journal of the Geotechnical Engineering Division 100, 763–786.

Lemaitre, J., Chaboche, J.L., 1990. Mechanics of Solid Materials. Cambridge University Press, New York.

Leon Bal, A.R., Hoppe, U., Dang, T.S., Hackl, K., Meschke, G., 2018. Hypoplastic particle finite element model for cutting tool-soil interaction simulations: Numerical analysis and experimental validation. Underground Space 3, 61–71. doi:10.1016/j.undsp.2018.01.008.

Li, C., Zhang, T., Goldman, D.I., 2013. A terradynamics of legged locomotion on granular media. Science 339, 1408–1412. doi:10.1126/science.1229163, arXiv:1303.7065.

Mary, B.C.L., Maillot, B., Leroy, Y.M., 2013. Deterministic chaos in frictional wedges revealed by convergence analysis. International Journal for Numerical and Analytical Methods in Geomechanics 37, 3036–3051.

McKyes, E., 1985. Soil cutting and tillage. Elsevier Scientific Publisher B. V., Amsterdam, The Netherlands. doi:10.1016/B978-0-444-88080-2.50013-2, arXiv:arXiv:1011.1669v3.

Milani, G., Lourenço, P.B., 2009. A discontinuous quasi-upper bound limit analysis approach with sequential linear programming mesh adaptation. International Journal of Mechanical Sciences 51, 89–104. doi:10.1016/j.ijmecsci.2008.10.010.

Mosek, 2015. The MOSEK optimization toolbox for MATLAB. MOSEK ApS.

Mroz, Z., 1967. On the description of anisotropic workhardening. Journal of the Mechanics and Physics of Solids 15, 163–175.

Osman, M.S., 1964. The mechanics of soil cutting blades. Journal of agricultural engineering research 9, 313–328.

Palmer, A., 1999. Speed effects in cutting and ploughing. Géotechnique 49, 285–294.

Perumpral, J.V., Grisso, R.D., Desai, C.S., 1983. A soil-tool model based on limit equilibrium analysis. Transactions of the ASAE 26, 0991–0995. doi:10.13031/2013.34062.

Petryk, H., 1983. A slip-line field analysis of the rolling contact problem at high loads. International Journal of Mechanical Sciences 25, 265–275. doi:10.1016/0020-7403(83)90030-9.

Prandtl, L., 1920. Über die härte plastischer körper. Nachr. K. Ges. Wiss. Göttingen., Math. Phys. Klasse , 74–85.

Prévost, J., 1977. Mathematical modelling of monotonic and cyclic undrained clay behaviour. International Journal for Numerical and Analytical Methods in Geomechanics 1, 192–216.

Raithatha, A., Duncan, S.R., 2009. Rigid plastic model of incremental sheet deformation using second-order cone programming. International Journal for Numerical Methods in Engineering 78, 955–979. doi:10.1002/nme.2512.

Randolph, M.F., 2004. Characterization of soft sediments for offshore applications, keynote lecture, in: Proc. Second International Conference on Geotechnical and Geophysical Site Characterization.

Randolph, M.F., Houlsby, G.T., 1984. The limiting pressure on a circular pile loaded laterally in cohesive soil. Géotechnique 34, 613–623.

Recuero, A., Serban, R., Peterson, B., Sugiyama, H., Jayakumar, P., Negrut, D., 2017. A high-fidelity approach for vehicle mobility simulation: Nonlinear finite element tires operating on granular material. Journal of Terramechanics 72, 39–54. doi:10.1016/j.jterra.2017.04.002.

Shi, Z., Hambleton, J.P., 2020. An r-h adaptive kinematic approach for 3D limit analysis. Computers and Geotechnics 124, 103531.

Stanier, S.A., White, D.J., 2013. Improved image-based deformation measurement in the centrifuge environment. Geotechnical Testing Journal 36, 1–14. doi:10.1520/GTJ20130044.

Sturm, J.F., 2002. Implementation of interior point methods for mixed semidefinite and second order cone optimization problems. Optimization Methods and Software 17, 1105–1154. doi:10.1080/1055678021000045123.

Tabor, D., 1959. Junction growth in metallic friction: the role of combined stresses and surface contamination. Proceedings of the Royal Society of London. Series

A. Mathematical and Physical Sciences 251, 378–393. doi:10.1098/rspa.1959.0114.

Terzaghi, K., 1943. Theorectical Soil Mechanics. John Wiley and Sons.

Tian, Y., Cassidy, M.J., 2010. The challenge of numerically implementing numerous force-resultant models in the stability analysis of long on-bottom pipelines. Computers and Geotechnics 37, 216–232. doi:10.1016/j.compgeo.2009.09.004.

Tsuji, T., Nakagawa, Y., Matsumoto, N., Kadono, Y., Takayama, T., Tanaka, T., 2012. 3-D DEM simulation of cohesive soil-pushing behavior by bulldozer blade. Journal of Terramechanics 49, 37–47. doi:10.1016/j.jterra.2011.11.003.

White, D., Dingle, H., 2011. The mechanism of steady friction between seabed pipelines and clay soils. Géotechnique 61, 1035–1041. doi:10.1680/geot.8.t.036.

White, D.J., Take, W.A., 2002. GeoPIV: Particle Image Velocimetry (PIV) software for use in geotechnical testing. Technical Report CUED/D-SOILS/TR322. Cambridge University, Engineering Department. Cambridge, United Kingdom. doi:10.7710/1093-7374.1624.

Xu, W., Zhang, L., 2019. Heat effect on the material removal in the machining of fibre-reinforced polymer composites. International Journal of Machine Tools and Manufacture 140, 1–11. doi:10.1016/j.ijmachtools.2019.01.005.

Yang, W.H., 1993. Large deformation of structures by sequential limit analysis. International Journal of Solids and Structures 30, 1001–1013.

Zhang, X., Krabbenhoft, K., Sheng, D., Li, W., 2015. Numerical simulation of a flow-like landslide using the particle finite element method. Computational Mechanics 55, 167–177.

Zhang, X., Wang, L., Krabbenhoft, K., Tinti, S., 2020. A case study and implication: particle finite element modelling of the 2010 Saint-Jude sensitive clay landslide. Landslides , 1–11.

Zhu, B., Dai, J., Kong, D., 2020. Modelling T-bar penetration in soft clay using large-displacement sequential limit analysis. Géotechnique 70, 173–180. doi:10.1680/jgeot.18.p.160.